BioNanoScience (2024) 14:643–660
https://doi.org/10.1007/s12668-024-01322-2

RESEARCH

A Comparative Study of PEGylated Cobalt Oxide Nanoparticles (Co_3O_4-NPs) and Cobalt Sulfide Nanoparticles (Co_9S_8-NPs) for Biological and Photocatalytic Applications

Muhammad Usman Zahid[1] · Muhammad Aslam Khan[1] · Uzair Ahmad[1] · Hanan Abdulaziz Alismail[2] · Syed Jawad Hussain[1] · Muhammad Irshad Khan[3] · Mohamed Soliman Elshikh[4] · Junaid Ihsan[5] · Syed Ali Imran Bokhari[1]

Accepted: 31 January 2024 / Published online: 17 February 2024

Abstract

Cobalt oxide nanoparticles (Co_3O_4-NPs) and cobalt sulfide nanoparticles (Co_9S_8-NPs) have shown extensive potential in electrochemical sensing, catalysis, specific drug targeting, and resonance imaging. However, Co_9S_8-NPs have been rarely explored for biomedical applications as compared to their oxide counterparts. Thus, in the current study, biocompatible PEGylated Co_9S_8-NPs and Co_3O_4-NPs are explored and compared for biological and photocatalytic properties. PEGylation of both the NPs is achieved using a simple chemical co-precipitation method followed by characterization using UV visible spectroscopy (UV-Vis), Fourier transform infrared spectroscopy (FTIR), X-ray diffraction (XRD), scanning electron microscopy (SEM), energy-dispersive X-ray analysis (EDX), and pH-responsive dispersion study. After thorough characterization, the NPs are evaluated and compared for various biological applications including antibacterial, antifungal, antileishmanial, antioxidant, and biocompatibility as well as photo-catalytic dye degradation studies. Both the NPs have shown excellent biological applications; however, Co_9S_8-NPs exhibit comparatively better antibacterial, antifungal, and antioxidant properties except antileishmanial potential where Co_3O_4-NPs show slight superiority. Furthermore, Co_3O_4-NPs indicate a higher degradation potential of methylene blue (MB) up to 46.93%. In comparison, Co_9S_8-NPs have a degradation ability of up to 42%, at 20 mg/ml within 3 h, which indicates considerable remediation potential of the NPs. Interestingly, both the NPs exhibit non-hemolytic behavior, thus demonstrating a compatible and bio-safe nature of both the NPs.

Keywords Cobalt oxide nanoparticles · Cobalt sulfide nanoparticles · PEGylation · Antimicrobial · Photocatalysis · Biocompatibility

1 Introduction

Advances in nanotechnology have compelled researchers to explore metallic nanoparticles in a wide range of applications. Cobalt oxide nanoparticles (Co_3O_4-NPs) possess

The authors Muhammad Usman Zahid and Muhammad Aslam Khan contributed equally to this work.

✉ Muhammad Aslam Khan
muhammadaslamkhanmarwat@gmail.com

✉ Syed Ali Imran Bokhari
ali.imran@iiu.edu.pk

[1] Department of Biological Sciences, Faculty of Sciences, International Islamic University (IIU), Islamabad, Pakistan

[2] King Abdullah International Medical Research Center (KAIMRC), King Saud bin Abdulaziz University for Health Sciences (KSAU-HS), Riyadh, Saudi Arabia

[3] Department of Chemistry, Faculty of Science, Allama Iqbal Open University, Islamabad, Pakistan

[4] Department of Botany and Microbiology, College of Science, King Saud University, P.O. 2455, Riyadh 11451, Saudi Arabia

[5] Department of Advanced Materials Chemistry, Korea University, Sejong 339-700, Republic of Korea

unique physical properties such as large surface area, strong conductivity, and high magnetization, making them promising materials while cobalt sulfide nanoparticles (Co_9S_8-NPs) are less toxic, and potentially suitable material for a wide array of applications [1, 2]. Because of their versatile properties, Co_3O_4 and Co_9S_8 NPs are used in energy storage, electrochemical sensing, magnetism, water splitting, batteries, catalysis, and energy production [3–9].

Cobalt complexes (Co_3O_4, Co_9S_8) have also shown extensive potential for biomedical applications such as magnetic resonance imaging, cell labeling, visualization of tissues and orthopedic implants, and as delivery vehicles for anticancer drugs as summarized in Table 1 [20–29]. Furthermore, Co_9S_8 also exhibits excellent sensing properties; for instance, numerous composites of Co_9S_8-NPs have shown potential for the detection of glucose and dopamine, a neurotransmitter released by the brain [30, 31].

Currently, various approaches are available to synthesize Co_3O_4-NPs and Co_9S_8-NPs including physical, chemical, and green methods [16, 32]. In the green method, biomass such as plants and microbes or their extracts are used as a reducing or stabilizing agent for the synthesis of NPs and thus considered a less toxic, cheap, and eco-friendly approach. However, there are a couple of drawbacks associated with the approach, mainly low yield, non-uniformity of the NPs, and reproducibility of the reactions. Similarly, mechanical methods use high energy and pressure to synthesize NPs. While mechanical methods may exhibit some pros such as high purity and uniform size of the NPs, the approach is also associated with some cons including high costs, labor, and use of high energy, temperature, and radiation exposure. In comparison to green and physical methods, chemical synthesis involves the interaction of atoms and smaller molecules at subnanometric scale, and the precursor metallic ions are converted into stable nanoparticles via nucleation and growth. In the method, suitable water-soluble reducing and capping agents are employed according to the need. The chemical approach is widely used for the synthesis of metallic nanoparticles because the method proves to be economical, facile, and highly controllable; gives a high yield of NPs with significant purity; and often leads to NPs with uniform size and shapes [17, 33–35].

PEGylation is the alteration of peptide, protein, and non-peptide molecules by adding one or more molecules of polyethylene glycol [36, 37]. PEGylation of the drugs/particles is mainly performed to extend the circulation period in the body, increase the solubility of drugs or dispersion of the NPs, decrease the effect of metabolic enzymes, and enhance drug stability [38]. The chemically synthesized, PEGylated metal nanoparticles have been explored as a contrast agent in imaging, and theranostics, and as carriers for targeted drug delivery, anti-inflammatory, cellular uptake, and biocompatibility evaluation [39–42].

Due to the unique biomedical properties of metallic oxides (such as Co_3O_4), extensive research has already been done but metallic sulfides (such as Co_9S_8) have always been ignored. Hence, there is a huge research gap or lack of literature for biomedical applications of Co_9S_8 which can be fulfilled by understanding the potential biological properties of Co_9S_8-NPs. By analyzing a few published research papers on Co_9S_8, it is clear that sulfides are excellent biosensors and their ability can be improved by either modifying their surface or using composites along them. Thus, herein, we have compared the potential biological properties of PEGylated cobalt oxide and cobalt sulfide nanoparticles. The particles were well characterized using multiple techniques using UV-Vis spectroscopy, FTIR, XRD, scanning electron microscope (SEM), and pH-responsive dispersion. Following, the particles were explored for varied biological properties using antibacterial, antifungal, antileishmanial, antioxidant, and compatibility studies.

Table 1 Previous studies on the biological applications of cobalt oxide and cobalt sulfide nanoparticles

Type of NPs	Precursor salt	Reducing/capping agents	Size (nm)	Shape	Applications	References
Co_3O_4-NPs	Cobalt nitrate hexahydrate	*Populus ciliata (leaves)*	25–35	Square	Antibacterial	[10]
Co_3O_4-NPs	Cobalt sulfate	*Piper nigrum*	51	Cubic	Antibacterial, antioxidant	[11]
CoO-NPs	Cobalt nitrate hexahydrate	*(Phoenix dactylifera) seeds*	80	Spherical	Antimicrobial, photocatalytic	[12]
Co_3O_4-NPs	Cobalt nitrate hexahydrate	*Rhodophyta*	29	Spherical	Antimicrobial, anticancer, anticoagulant, antioxidant	[13]
CoO-NPs	Cobalt chloride	*Curcuma longa (roots)*	80	Spherical	Antioxidant, photocatalytic, antitumor	[14]
Co_3O_4-NPs	Cobalt chloride hexahydrate	*Citrus limon*	Nil	Pyramid-like crystal	Antimicrobial	[15]
Co_3O_4-NPs	Cobalt(II) acetate tetrahydrate	Salicylaldehyde	30–50	Spherical	Nil	[16]
CoO-NPs	Cobalt nitrate hexahydrate	*Punica granatum*	40–80	Spherical	Photocatalytic	[17]
Co_3O_4-NPs	Cobalt chloride	Urea	20–25	Non-spherical	Anti-apoptotic marker, antimicrobial	[18]
CoS	Cobalt sulfate	Sodium sulfide	Nil	Nil	Antimicrobial, photocatalytic	[19]

2 Experimental

2.1 Materials

2.1.1 Chemicals and Reagents

Cobalt(II) nitrate hexahydrate $Co(NO_3)_2{\cdot}6H_2O$ (97%) was purchased from Samchun Pure Chemical Co., Ltd. Sodium borohydride ($NaBH_4$) poly(ethylene glycol)-6000, and sodium sulfide nonahydrate ($Na_2S{\cdot}9H_2O$) were acquired from Sigma-Aldrich. All the chemicals were utilized as received without any additional purification. Distilled water was used throughout the experiments to avoid impurities.

2.2 Methodologies

2.2.1 Synthesis Co_3O_4-NPs

In a typical experiment, $Co(NO_3)_2{\cdot}6H_2O$ was used as a precursor to synthesize nanoparticles. Briefly, a 0.0625 M solution of $Co(NO_3)_2{\cdot}6H_2O$ was prepared by adding 1.82 g of salt into 100 ml of distilled water. 1.82 g of poly(ethylene glycol) was also dissolved in 100 ml of distilled water, in a separate flask. After a continuous stirring for 15 min, poly(ethylene glycol) solution was added dropwise into the precursor salt solution. After complete addition and mixing, the temperature of the mixture was risen and maintained at 65 °C. Next, a 0.125 M solution (0.473 g) of $NaBH_4$ (reducing agent) was prepared in 100 ml distilled water and added to the mixture drop-by-drop. A color change from black to green was observed with the addition of a reducing agent. The final solution was continuously stirred at 65°C for 4 h. The precipitate obtained was centrifuged and washed thrice at 4000 rpm, with distilled water. The product was then dried in the oven overnight, collected after drying, and ground in mortar and pestle. Finally, the NPs were calcined in a muffle furnace at 450 °C for 2 h to increase the crystalline nature, and crystallite size and to remove any contaminants from the sample [43].

2.2.2 Synthesis of Co_9S_8-NPs

Similar to the synthesis of Co_3O_4-NPs, Co_9S_8-NPs were also synthesized by chemical precipitation method. Initially, 0.0625M (1.82g) $Co(NO_3)_2{\cdot}6H_2O$ and 0.125M (3.015 g) of sodium sulfide nonahydrate ($Na_2S{\cdot}9H_2O$) solutions were prepared by dissolving each chemical into 100 ml of distilled water, in separate flasks. After 15 min of continuous stirring, both solutions were mixed and stirred for 15 min. In the second step, 1.82 g of poly(ethylene glycol) solution was prepared in 100 ml distilled water and added to the mixture. After complete mixing, the temperature of the flask was raised and maintained at 65 °C, with continuous stirring. In the final step, 0.125 M (0.473 g) of $NaBH_4$ solution was prepared in 100 ml distilled water and was added dropwise into the mixture. The final solution was continuously stirred at 65 °C for 4 h. The precipitate obtained was centrifuged and washed thrice at 4000 rpm, with distilled water. The final product was dried in the oven overnight, collected after drying, ground in mortar and pestle, and calcined in a muffle furnace at 450 °C for 2 h.

2.2.3 Characterization

Several characterization techniques, including X-ray diffraction (XRD), Fourier transform infrared spectroscopy (FTIR), SEM, and energy-dispersive X-ray analysis, were used for physiological and morphological characterization. In UV-Vis spectroscopic measurement, NP dispersion was prepared as 0.25 mg/ml in dH_2O, and absorption was recorded from 280 to 800 nm. Functional groups and PEG capping were detected by FTIR analysis in wavelengths of 500–4000 cm^{-1}. The crystallinity of NPs (Co_3O_4 and Co_9S_8) was detected by an X-ray diffractometer supplied with Cu and Kα as sources of radiation, and Ni as a filter with 45 kV energy. The characterization was conducted at a scan rate of 5°/min from 20° to 85°. Crystallite size was evaluated by using the Debye–Scherer formula [44].

$$D = k\lambda/(\beta \cos \theta)$$

Surface morphology and size of NPs were observed by using a scanning electron microscope at an accelerating voltage of 15 kV. Energy-dispersive X-ray analysis of NPs was performed to analyze the atomic constituents of Co_3O_4-NPs and Co_9S_8-NPs.

2.2.4 pH-Responsive Dispersion Studies

To assess the dispersion capability of Co_3O_4-NPs and Co_9S_8-NPs, a pH-responsive dispersion activity was carried out. Five milligrams/15 mL dilutions were made in vials at different pH values (2, 7, and 12) and subjected to sonication for 30 min. Over the following 24 h, the resultant dilutions were monitored for dispersion activity, and color changes were documented using images taken instantaneously after sonication, after 10 min, 30 min, 1 h, 2 h, 6 h, and 24 h.

2.3 Biological Applications

2.3.1 Antibacterial Assay

In the study, the antibacterial activity of chemically synthesized Co_3O_4-NPs and Co_9S_8-NPs was performed in

triplicates by the well diffusion method against two gram-positive and three gram-negative bacterial strains including *Bacillus subtilis* (ATCC-6633), *Staphylococcus aureus* (ATCC-6538), *Klebsiella pneumonia* (ATCC-1705), *Escherichia coli* (ATCC-25922), and *Pseudomonas aeruginosa* (ATCC-15442). Nutrient agar plates were streaked with cotton swabs with 100 µl bacterial strains and allowed to dry for 5 min. Wells were made in the plates and named as A, B, C, D, negative (−ve), and positive (+ve). Different dilutions (40 mg/ml, 20 mg/ml, 10 mg/ml, and 5 mg/ml) of the NPs were made in DMSO and sonicated for 20 min. Wells were then filled with dilutions in such a way that well A contains 40 mg/ml, 20 mg/ml in well B, 10 mg/ml in well C, 5 mg/ml in well D, and positive control (Levofloxacin) in the central well. DMSO was used as a negative control in the test. After incubation of plates at 37 °C for 24 h, the zone of inhibition (ZOI) was measured in millimeters (mm) using a measurement scale. Minimum inhibitory concentration (MIC) was also evaluated to screen the minimum inhibitory potential of the NPs.

2.3.2 Antifungal Assay

This activity was performed to assess the antifungal potential of Co_3O_4-NPs and Co_9S_8-NPs against three fungal strains including *Aspergillus terreus* (FCBP-0058), *Trichophyton rubrum*, and *Aspergillus flavus* (FCBP-0064), by a well diffusion method [45]. Fungal spores were harvested in Tween 20 solutions. Sabouraud dextrose agar (SDA) plates were streaked by cotton swabs with 100 µL fungal spore suspension and allowed to dry for 5 min. Wells were made and filled with NP dilutions (80 mg/ml, 40 mg/ml, 20 mg/ml, and 10 mg/ml). The antifungal drug (clotrimazole) was used as positive control and DMSO was used as a negative control, the plates were then incubated at 27 °C for 48–72 h and ZOI was measured in millimeters (mm) by measurement scale.

2.3.3 Antileishmanial assay

The nanoparticles were examined for leishmanicidal activity against *Leishmania tropica-KWH23*. The capability of the NPs was evaluated against both flagellated (promastigote) and non-flagellated (amastigote) phases of the dimorphic parasite. Both parasitic test subjects were freshly cultivated and retained in a specialized medium (10% FBS) for 12 h, according to the protocol [46]. Later on, 180 µl of the renewed promastigote and amastigote cultures and 10 µl of the NP samples (12.5–200 µg/ml), under consideration, were perfectly mixed in designated wells of the 96-well plate, followed by an incubation of 72 h at 28°C. The NPs were perfectly dissolved in DMSO and used as the negative control, and Amphotericin-B was used as a positive control. After a 72-h incubation period, 10 µl of the MTT solution (5 mg/ml) was added into the wells, followed by a 4-h re-incubation (28 °C). The absorbance was analyzed at 560 nm and the activity was measured as % inhibition,

$$\%\text{Inhibition} = \left[1 - \left\{ \frac{\text{Abs}}{\text{Abc}} \right\} \right] \times 100$$

Here Abs represents the absorbance of the samples under consideration and Abc represents the absorbance of the negative control.

2.3.4 Antioxidant Activities

DPPH Free Radical Scavenging Assay A typical procedure by Ihsan et al. (2021) was applied to quantify the potential free radical scavenging capability of DPPH [47]. In short, 20 µL of the NP dispersion (4 mg/ml) was merged with 180 µL of the DPPH reagent in the designated wells of a 96-well plate, followed by dark incubation of 2 h at 37 °C. After the incubation time, absorbance was measured at 517 nm, and each sample's free radical scavenging capability was evaluated using the formula.

$$(\%)\ \text{FRSA} = \left(\text{Abs control} - \frac{\text{Ab sample}}{\text{Abs control}} \right) \times 100$$

where control is the absorbance of DPPH solution without the test sample and Ab sample represents the absorbance of the test sample containing NPs and DPPH solution.

Total Reducing Power The assay was executed with various changes to the procedure used by Aziz et al. (2021) [48]. In brief, a reaction mix including 100 µl of the sample, 200 µl of phosphate buffer (pH 6.6), and 100 µl of potassium ferricyanide (1% w/v) was prepared in an Eppendorf tube. The tube was then incubated in a water bath for 45 min at 60 °C. After incubation, 200 µl of 10% w/v trichloroacetic acid was slowly added into the mixture and centrifuged at 3000 rpm for 15 min. The supernatant (150 µl) was carefully put into the appropriate well on the plate, which previously included 50 µl of ferric cyanide ($C_6N_6FeK_3$) solution (0.1% w/v). The samples' absorbance was evaluated at 630 nm.

2.3.5 Biocompatibility

A blood biocompatibility assay was performed against Co_3O_4-NPs and Co_9S_8-NPs to examine the hemocompatibility of the materials. Initially, 5 ml of fresh blood was taken from a healthy human with informed consent, centrifuged at 4000 rpm, washed twice with phosphate buffer saline (PBS), and re-suspended in PBS respectively. Then, a 2% EDTA solution was prepared and added to the blood to avoid coagulation. Four different concentrations (5 mg/ml, 2.5 mg/ml, 1.125 mg/ml, and 0.562 mg/ml) of NPs were

prepared and used to analyze the hemolysis of RBCs. Microscopic slides were prepared by adding 20 µl RBCs and NP dilutions. Triton X-100 was employed as a positive control while re-suspended RBCs in PBS were considered a negative control. After 1 h of incubation at 37 °C, slides were analyzed at 1000× magnification and micrographs were taken respectively.

2.4 Photocatalytic Applications

2.4.1 Dye Degradation Assay

The dye degradation assay was performed to analyze the photocatalytic capability of Co_3O_4-NPs and Co_9S_8-NPs. Methylene blue (MB), a cationic dye, was used as a control for this assay. Typically, a stock solution of MB dye (10 mg/l) was prepared and maintained at 26±1 °C. A total of 40 ml of MB dye was taken from the stock and 40 mg NPs was added to it in an Erlenmeyer flask. Constant stirring at 200 rpm was performed under direct sunlight. Sample aliquots were taken out at varying time intervals ranging from 0 to 180 min and centrifuged at 10,000 rpm for 8 min. The absorbance of supernatant, collected after centrifugation, was analyzed using a UV-Vis spectrophotometer. % degradation for MB dye was calculated using the equation [49].

$$\%(D) = \left(\frac{Co - C}{Co}\right) \times 100$$

Here, Co is the concentration of dye at 0 min while C is the concentration of dye at a specific time interval.

2.5 Statistical analysis

Two-way ANOVA was implemented in GraphPad Prism to analyze the statistical significance of antibacterial activity. Results were viewed as statistically significant if $P<0.05$ when comparing both NPs at the highest concentration of antibacterial activity. The data are presented as mean values from triplicates ($n=3$) with standard deviation (±SD).

3 Results and Discussion

3.1 Synthesis of Co_3O_4-NPs and Co_9S_8-NPs

$Co(NO_3)_2{\cdot}6H_2O$ was used as a precursor salt for the synthesis of Co_3O_4-NPs. The whole synthesis process was a series of color changes from pink to green. Initially, crystal clear poly(ethylene glycol) solution was added to the pink-colored $Co(NO_3)_2{\cdot}6H_2O$ solution, the pink color remained visible. Subsequently, the addition of $NaBH_4$, a reducing agent, turned the pink color into blackish, followed by fume formation. After continuous stirring at 65 °C for 4 h, the black color slowly turned green. The greenish mixture was then washed, dried, and later on collected. Calcination at 450 °C for 2 h provided black-colored Co_3O_4-NPs. Initially, the dissociation of $Co(NO_3)_2{\cdot}6H_2O$ in water results in the formation of $Co(OH)_2$. The obtained $Co(OH)_2$ interacts with PEG to create a $Co(OH)_2$-PEG complex as depicted in Fig. 1. The reaction mixture was eventually treated with $NaBH_4$, which converted Co_2^+ ions to Co atoms. The Co atoms interact with the $Co(OH)_2$-PEG complex, leading to the formation of Co_3O_4-NPs. The resulting $Co(OH)_2$-PEG-Co_3O_4 mixture was calcined, converting the $Co(OH)_2$ to Co_3O_4-NPs [50]. In the reaction, PEG worked as a stabilizing agent which prevented the destabilization of Co_3O_4-NPs.

Similarly, Co $(NO_3)_2$ $6H_2O$ was also used as a precursor salt for the synthesis of Co_9S_8-NPs. Initially, solutions of $Co(NO_3)_2{\cdot}6H_2O$ and Na_2S were mixed after stirring separately. The green color appeared which eventually turned

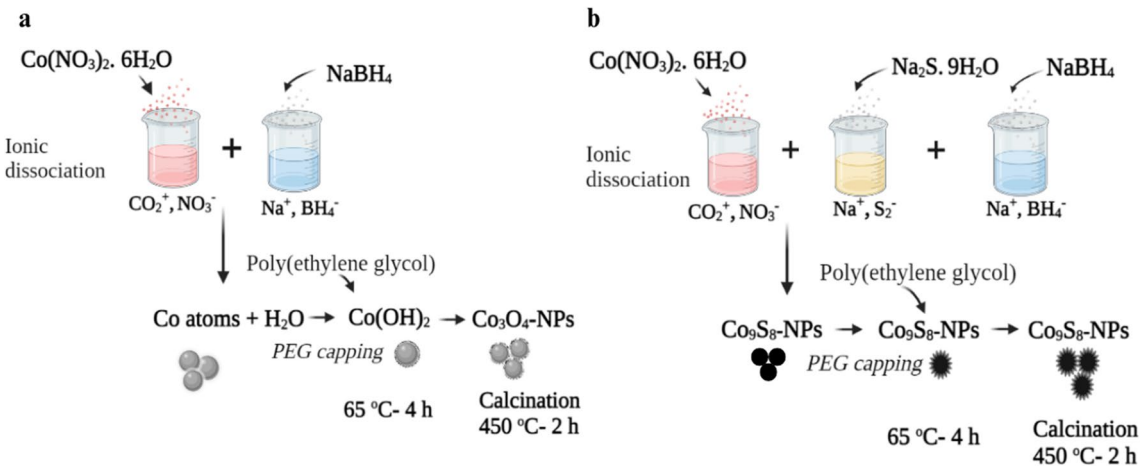

Fig. 1 Schematic illustration of the possible mechanism of synthesis of **a** Co_3O_4-NPs and **b** Co_9S_8-NPs

brownish-green after the addition of poly(ethylene glycol). The addition of $NaBH_4$ turned the brownish-green color of the solution into blackish, followed by fume formation. After 4 h of continuous stirring at 65°C, the NPs were washed, dried, and later on collected. The $Co(NO_3)_2{\cdot}6H_2O$ and $Na_2S{\cdot}9H_2O$ dissolved in water produce Co_2^+ and S_2^- ions, which are then utilized to synthesize Co_9S_8-NPs. These ions combine to produce CoS nuclei, which grow when additional sulfur and PEG are utilized. Co_2^+ ions turn into Co atoms when $NaBH_4$ is added, producing a mixture of CoS and Co nanoparticles. However, when there is excessive sulfur in the reaction mixture, more and more Co atoms react with sulfur atoms to produce Co_9S_8-NPs [50]. In the synthesis, PEG worked as a stabilizing agent during the synthesis process.

3.2 Characterization

3.2.1 UV-VIS Spectroscopy

The optical characterization was performed by analyzing the absorption and transmittance of Co_3O_4-NPs and Co_9S_8-NPs as illustrated in Fig. 2. For Co_3O_4-NPs, the absorption spectrum showed a slight absorption within the wavelength of 280–500 nm indicating the presence of surface plasmon resonance (SPR) [51]. The SPR peak was most likely influenced by the crystallite size of Co_3O_4-NPs [51]. However, Co_9S_8-NPs showed no absorption peak in the entire visible region. This is more likely to be due to the size of Co_9S_8-NPs [51]. The measurement of transmittance is a highly valuable tool to analyze the ability of NPs to transmit light. In the case of Co_9S_8-NPs, transmittance increased rapidly at around 300 nm (λ) and as the wavelength increased above 300 nm, the absorption band shifted towards longer wavelengths (red-shifted), causing the peaks on the transmittance graph to rise to higher values. However, Co_3O_4-NPs showed low transmittance throughout the entire wavelength range with slight peaks at 320 nm and 620 nm. The transmittance of Co_9S_8-NPs and Co_3O_4-NPs was more likely to be influenced by NP size [52].

3.2.2 FTIR Analysis

Molecular structure and functional group analysis of Co_3O_4-NPs and Co_9S_8-NPs were performed by FTIR spectroscopy. FTIR spectra of Co_3O_4-NPs displayed eminent peaks at 564.1, 662.26, 1104.99, 1354.85, and 3362.87 cm^{-1} as shown in Fig. 3. The spectra showed two distinct and strong absorption bands at 564.1 cm^{-1} and 662.26 cm^{-1}, originating from fingerprint vibrational stretching of Co–O bonds in Co_3O_4-NPs. It also confirmed the spinel crystal structure of Co_3O_4-NPs. Bands at 1104.99 cm^{-1}, 1354.85 cm^{-1}, and 3362.87 cm^{-1} were observed, attributed to C–O, Co–O, and C–OH stretching respectively, which confirmed the PEG coating on Co_3O_4-NPs [53]. Contrary to Co_3O_4-NPs, FTIR spectra of Co_9S_8-NPs displayed prominent peaks at 559.66, 660.1, and 1127 cm^{-1}. The spectra showed two sharp bands at 559.66 cm^{-1} and 660.1 cm^{-1}, originating from fingerprint vibrational stretching of Co–S and S–Co–S bonds in Co_9S_8-NPs. Another slight band was observed at 1127 cm^{-1}, attributed to C–O–C stretching, which confirmed the PEG coating on Co_9S_8-NPs [44].

3.2.3 XRD Analysis

The phase structure and crystallite size of PEGylated Co_3O_4-NPs and Co_9S_8-NPs were evaluated by an X-ray diffractometer, in a 2θ range of 20° to 85°, operated with Cu as an anode using 45-kV energy. XRD patterns of Co_3O_4-NPs as shown in Fig. 4 a displayed spinel crystal structure (JCPDS No: 76-1802) with the diffraction peaks at 2θ values of 37.09°, 38.42°, 65.06°, and 78.20° which correspond to (311), (222), (440), and (533), planes respectively [54]. The average crystalline size of Co_3O_4-NPs as measured by the Debye–Scherer formula was calculated to be 39.86 nm [3], whereas for Co_9S_8-NPs, diffraction peaks at 2θ values of 24°, 31.4°, 34.4°, 36.7°, 38.3°, 44.7°, and 59.3° were obtained which corresponded to (200), (311), (222), (400), (331), (422),

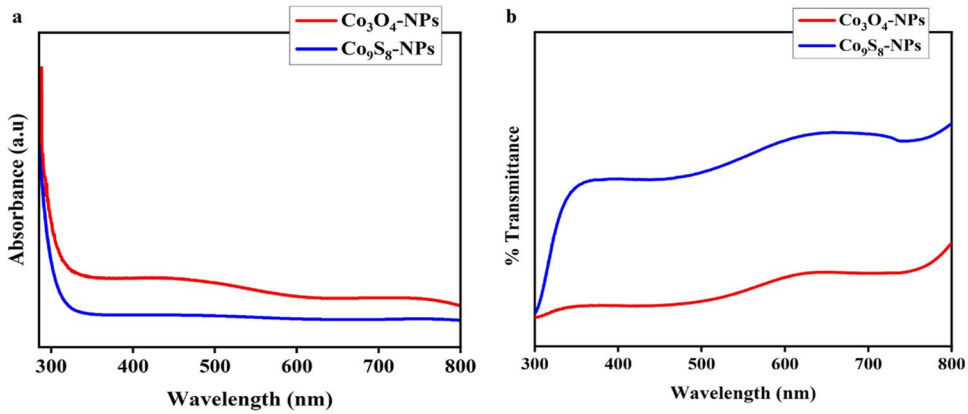

Fig. 2 UV-Vis spectra of Co_3O_4-NPs and Co_9S_8-NPs. **a** Absorbance spectra, **b** transmittance spectra

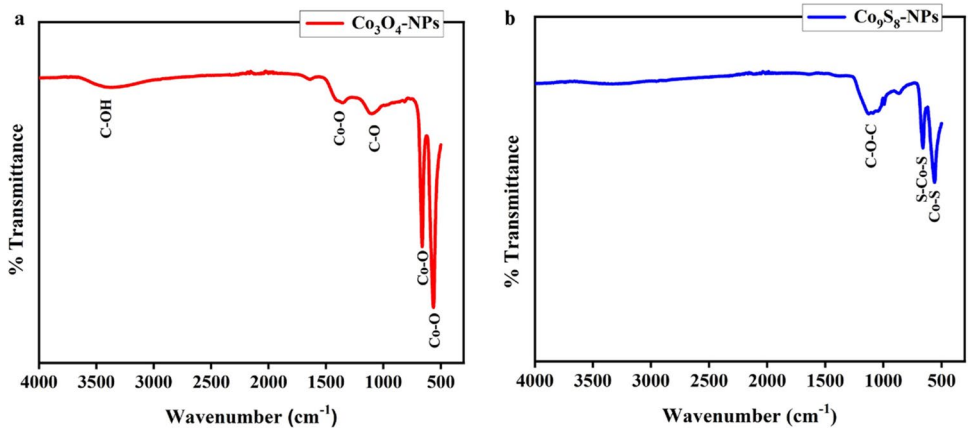

Fig. 3 FTIR spectra of **a** Co_3O_4-NPs and **b** Co_9S_8-NPs

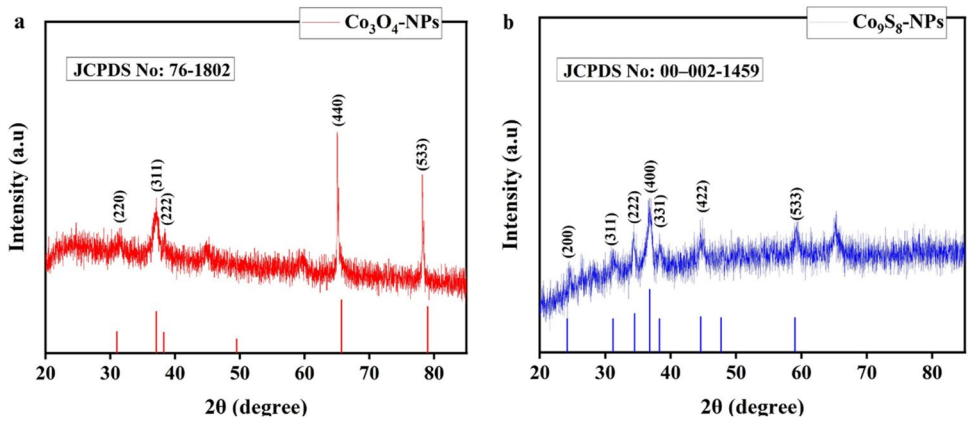

Fig. 4 XRD diffraction patterns of **a** Co_3O_4-NPs and **b** Co_9S_8-NPs

and (533) planes, respectively [55]. A slight deflection from exact peaks was observed which may be due to intense PEG coating on the surface of NPs. The XRD pattern of PEGylated Co_9S_8-NPs thus displayed cubic crystal structure (JCPDS No: 00-002-1459) and the average crystallite size of the NPs as measured by Debye-Scherer formula was calculated to be 36.7 nm [56].

3.2.4 Morphological and Elemental Studies

Morphological exploration of chemically synthesized PEGylated Co_3O_4-NPs and Co_9S_8-NPs was performed using a SEM as displayed in Fig. 5 a and b. SEM analysis of both the Co_3O_4-NPs and Co_9S_8-NPs showed slight agglomeration in particular in Co_3O_4-NPs. Overall Co_9S_8-NPs showed spherical or elliptical morphology while Co_3O_4-NPs displayed relatively high agglomeration with elliptical or irregularly shaped morphology of the NPs. The average size for Co_9S_8-NPs as computed with ImageJ was 63.3±14.92 nm while the mean size for Co_3O_4-NPs was determined as 41.67±6.80 nm. Comparatively, Co_9S_8-NPs displayed smooth surface morphology, making it easier for NPs to make strong contact with bacterial cell walls thus enhancing their potential antimicrobial activity. This kind of behavior of smooth-surfaced NPs has already been demonstrated in previous literature [10].

The elemental composition analysis of PEGylated Co_3O_4-NPs and Co_9S_8-NPs was performed by EDX spectroscopy as shown in Fig. 5c and d. The EDX spectra of Co_3O_4-NPs showed that the required amount of Co and O are present in NPs which confirmed the formation of highly pure Co_3O_4-NPs. Weight % of O and Co elements were determined as 32.56% and 67.44% while atomic % was determined as 64% and 36%, respectively. For Co_9S_8-NPs, EDX spectra confirmed the formation of Co_9S_8-NPs because of the presence of S and Co elements. The weight % of S and Co elements was evaluated as 11.82% and 88.18% while atomic % was evaluated as 18.31% and 81.69%, respectively. The current data thus confirms the formation of Co_3O_4-NPs and Co_9S_8-NPs.

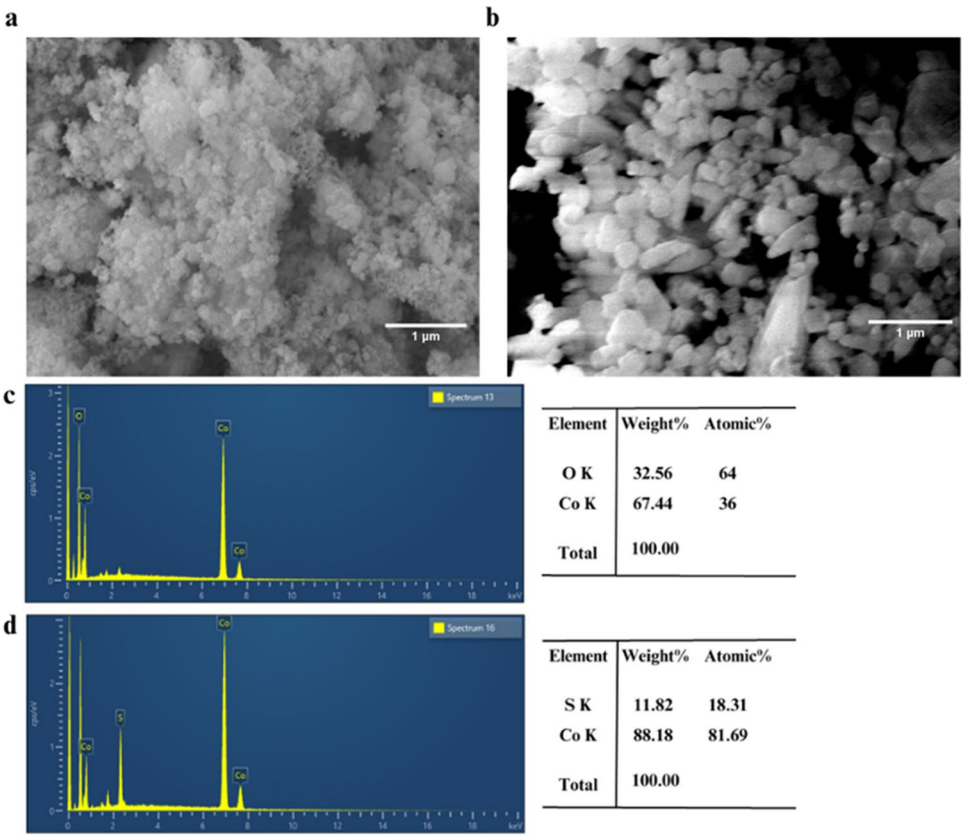

Fig. 5 SEM micrographs of **a** Co_3O_4-NPs and **b** Co_9S_8-NPs and EDX analysis of **c** Co_3O_4-NPs and **d** Co_9S_8-NPs

3.2.5 pH-Responsive Dispersion Study

Dispersion studies are prominent in nanotechnology since they influence the characteristics and behavior of nanoparticles in diverse applications. Optimal dispersion improves performance, but inadequate dispersion yields unsatisfactory outcomes. Dispersion study provides insight into the interactions of nanoparticles with their surroundings, assuring repeatability, biocompatibility, and comparability of experimental techniques [57]. In the current study, Co_3O_4-NPs and Co_9S_8-NPs displayed similar dispersion activity in distilled water, with both NPs being completely dispersed after sonication as presented in Fig. 6. However, the commencement of sedimentation began after 10 min, and all the NPs, except for Co_3O_4-NPs and Co_9S_8-NPs at pH 2, were mostly sedimented within an hour after sonication. After 6 h, all NPs at varying pH levels (2, 7, and 12) were completely sediment. However, Co_3O_4-NPs and Co_9S_8-NPs showed good dispersion capability at pH 2, as they remained dispersed even after 2 h, whereas none of the other NPs remained dispersed.

3.3 Biological Applications

3.3.1 Antibacterial Studies

Antibacterial nanomaterials can be used to prevent the growth and propagation of bacteria in a wide range of applications, including diagnostic instruments, wound dressings, and textiles. They are essential for limiting infection risk and boosting cleanliness in a variety of settings [45, 58]. In the current study, the antibacterial activity of PEGylated Co_3O_4-NPs and Co_9S_8-NPs was studied against two gram-positive, i.e., *B. subtilis* and *S. aureus*, and three gram-negative bacterial strains, i.e., *K. pneumonia*, *E. coli*, and *P. aeruginosa*. An agar well diffusion assay was used to explore the antibacterial potential of the samples with Levofloxacin and DMSO as positive and negative controls, respectively. In the study, both the NPs showed dose-dependent effectiveness but Co_9S_8-NPs showed more efficient antibacterial activity as compared to Co_3O_4-NPs as displayed in Table 2 and Fig 7. For instance, at the highest tested concentration of 40 mg/ml, Co_9S_8-NPs displayed maximum zone of inhibition (ZOI) against *P. aeruginosa* which was measured as 24±1 mm. *B. subtilis* was found to be the second most sensitive strain to Co_9S_8-NPs as it resulted in 22±1.4 mm ZOI. At a similar concentration, *K. pneumonia* showed a ZOI of 20±1.5 mm. Although *K. pneumonia* showed comparatively lower ZOI for Co_9S_8-NPs at 40 mg/ml, it was still found to be more sensitive at a lower concentration as it resulted in 13±1 mm ZOI at 1.25 mg/ml. Similarly, *S. aureus* induced ZOI of 21±1.2 mm at 40 mg/ml, and its MIC was observed to be 1.25 mg/ml. Among the tested strains, *E. coli* was examined to be the least sensitive as it induced 20.5±1.1

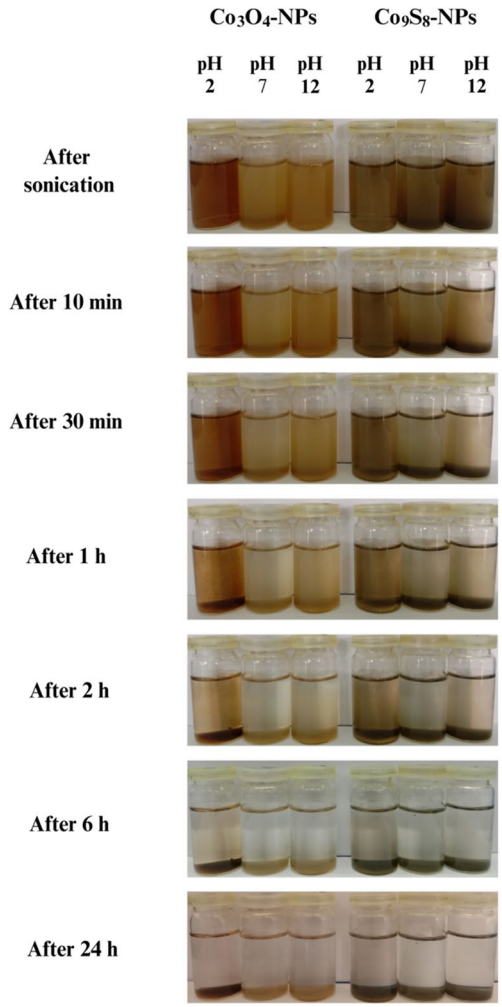

Fig. 6 Pictorial presentation of pH-responsive study of Co_3O_4-NPs and Co_9S_8-NPs at varied pH

mm ZOI at 40 mg/ml with a MIC of 5 mg/ml. Contrary to Co_9S_8-NPs, Co_3O_4-NPs resulted in a comparatively higher zone of inhibitions but with higher MICs. For instance, at the highest tested concentration of 40 mg/ml, Co_3O_4-NPs exhibited maximum ZOI against *E. coli* which was measured as 28±1.1 mm. *B. subtilis* was found to be the second most sensitive strain to Co_3O_4-NPs as it resulted in 24±1.4 mm ZOI. At a similar concentration, *S. aureus* showed a ZOI of 19±1.2 mm. Although *S. aureus* showed comparatively lower ZOI for Co_3O_4-NPs at 40 mg/ml, it was still found to be more sensitive at a lower concentration as it resulted in 9±1.2 mm ZOI at 2.5 mg/ml. Similarly, *K. pneumonia* induced ZOI of 19±1.6 mm at 40 mg/ml, and its MIC was observed to be 5 mg/ml. Among the tested strains, *P. aeruginosa* was examined to be the least sensitive as it induced 22±1.2 mm ZOI at 40 mg/ml with MIC of 10 mg/ml.

A comprehensive literature review reveals that metallic nanoparticles (MNPs) inhibit bacterial growth in multiple ways as illustrated in Fig 8. Once NPs come into contact with bacteria, they can pass through the cell membranes, obstruct metabolic processes, and affect the morphology of membranes. Once inside the cells, NPs interfere with the cellular machinery of the microbes to suppress enzyme activity, diminish protein function, induce oxidative stress, promote electrolyte imbalances, and influence gene expression levels. The cell dies as a result of the release of cellular matrix and damage to organelles caused by the creation of pits in the cell membrane [59, 60].

3.3.2 Antifungal Studies

The antifungal activity of PEGylated Co_3O_4-NPs and Co_9S_8-NPs was studied against three fungal strains, i.e., *A. terreus*, *T. rubrum*, and *A. flavus.* These strains are clinically important because they are usually associated with multiple human fungal infections such as invasive aspergillosis, tinea pedis, tinea cruris, and aflatoxicosis [61]. An agar well diffusion method in various concentrations was used to examine the fungicidal activity of Co_3O_4-NPs and Co_9S_8-NPs. Interestingly, Co_3O_4-NPs did not show any activity against any of the fungal strains used as displayed in Fig 9. Contrary to Co_3O_4-NPs, Co_9S_8-NPs at the highest tested concentration of 80 mg/ml induced the highest zone of inhibition (ZOI) of 19±1.2 mm against *A. flavus*. *A. terreus* also resulted in moderate sensitivity against Co_9S_8-NPs with a ZOI of 14±1 mm. Furthermore, the least sensitive fungal strain was *T. rubrum*, which showed ZOI of 10±1 mm at 80 mg/ml. However, it is noteworthy that the particles were only active at the highest concentration against the tested fungal strains as the strains only displayed sensitivity at 80 mg/ml.

A complex mechanism may be involved in the antifungal activity of cobalt nanoparticles as illustrated in Fig 10. Initially, when the NPs interact with fungi, metal ions are released, which bind to particular protein groups on the fungal cells. The metal ions emitted are determined depending on the type of NPs and fungus involved. This interaction can cause electron transport disruption, membrane potential abnormalities, reduced protein function, enhanced oxidative stress, electrolyte imbalance, abnormal gene expression, and poor nutritional absorption. Metal ions from NPs also cause DNA damage, resulting in cellular death [62].

3.3.3 Antileishmanial Studies

Leishmania is a highly neglected parasitic disease that is common in tropical and subtropical areas and affects humans and animals worldwide. The disease is widespread and is caused by the bite of an infected female sandfly [1]. Cutaneous leishmaniasis is caused by a protozoan parasite *Leishmania tropica*. During infection, the parasite experiences two stages: the extracellular promastigote stage, which resides

Table 2 Antibacterial activity of Co_9S_8-NPs and Co_3O_4-NPs at various concentrations with MICs

Sample	Conc.	Zone of inhibition (mm) Bacterial strains				
		K. pneumonia	*P. aeruginosa*	*E. coli*	*S. aureus*	*B. subtilis*
Co_9S_8-NPs	40 mg/ml	20±1.6	24±1.0	20.5±1.4	21±1.2	22±1.4
	20 mg/ml	19±1.2	22±1.0	19±1.2	20±1.0	19±1.4
	10 mg/ml	18±1.0	20±0.8	17.5±1.2	16±1.0	15.5±1.2
	5 mg/ml	17±0.8	19±0.8	15.5±1.0	14.5±0.8	14±1.2
MIC (mg/ml)		1.25	5	5	1.25	2.5
PC		29±1.8	30±1.2	27±1.6	25±2	26±2
NC		--	--	--	--	--
Co_3O_4-NPs	40 mg/ml	19±1.6	22±1.2	28±1.1	19±1.2	24±1.4
	20 mg/ml	17±1.3	15±1.1	19±1.0	17±1.1	18±1.2
	10 mg/ml	16±1.3	12.5±1.0	18±1.0	15±1.2	17±1.2
	5 mg/ml	13±0.8	--	9±0.8	10±1.2	13±1.0
MIC (mg/ml)		5	10	5	2.5	5
PC		27±1.8	21±1.2	35±1.6	27±2	25±2
NC		--	--	--	--	--

PC stands for positive control while NC denotes negative control. The symbol "--" indicates no observed results

in the sand fly's abdomen, and the intracellular amastigote stage, which propagates inside host cells. The amastigote stage is chiefly responsible for clinical symptoms, which include skin lesions, scarring, and ulcers [46].

In the study, the leishmanicidal efficacy of Co_3O_4-NPs and Co_9S_8-NPs was examined against *Leishmania tropica* using multiple concentrations that included 12.5, 25, 50, 100, and 200 µg/ml. An MTT cell viability assay was conducted to evaluate the growth inhibition of promastigote and amastigote when incubated with NP dilutions. Concentration-dependent growth inhibition was documented as shown in Fig. 11. Although all the tested NP concentrations displayed excellent growth suppressive effects, % inhibition increased with an increase in NP concentration. Comparatively, Co_3O_4-NPs showed higher % inhibition than Co_9S_8-NPs, at the highest tested concentration but at lower concentrations, Co_9S_8-NPs displayed more potential than Co_3O_4-NPs. For Co_3O_4-NPs, the highest tested concentration (200 µg/ml) resulted in 77.40±1.2% and 69.34±1.2% inhibition for promastigote and amastigote, respectively. However, it reduced to 4.21±1.0% and 2.12±1.2% when dealing with the lowest tested concentration (12.5 µg/ml). Furthermore, the IC_{50} was measured for promastigote and amastigote as 110.33 µg/ml and 141.2 µg/ml, respectively. Subsequently, for Co_9S_8-NPs, the highest tested concentration resulted in 72.3±1.4% and 68.2±1.2% inhibition for promastigote and amastigote, respectively. When dealing with the lowest concentration, % inhibition was reduced to 10.78±1% and 9.42±1.2%, respectively. The IC50 was determined for promastigote and amastigote as 95.21 µg/ml and 128.5 µg/ml, respectively.

The antileishmanial mechanism can be hypothesized as reported for other metallic nanoparticles as illustrated in Fig. 12. Initially, the MNPs interact with the parasite's membrane, penetrate it, produce reactive oxygen species (ROS), and induce oxidative stress (OS) which ultimately leads to cell death. The ultra-small dimension and high surface area give NPs an interesting opportunity to interact with sensitive and delicate parts of cells, DNA, and enzymes which lead to faulty protein synthesis and enzyme inactivity and thus lead to parasite mortality [63].

3.3.4 Antioxidant Studies

The antioxidant ability of PEGylated Co_3O_4-NPs and Co_9S_8-NPs was analyzed by DPPH (2,2-diphenyl-1-picrylhydrazyl)-free radical scavenging activity, and total reducing power (TRP) activity as summarized in Fig 13. Free radical scavenging ability was evaluated by using DPPH-FRSA at 500 µg/ml. The stable free radical DPPH has a prominent absorption at 517 nm and a deep purple appearance. When an antioxidant that scavenges free radicals interacts with DPPH, it transforms it into the less absorbent/colorless stable DPPH solution. As the DPPH free radical gains electrons from the antioxidant molecules, decolorization (yellow hue) of the purple DPPH solution emerges [64]. In the study, Co_9S_8-NPs displayed superior free radical scavenging ability, with 22.35±0.4% inhibition of the DPPH, whereas Co_3O_4-NPs showed only 5.81±0.6% DPPH inhibition. To further affirm the antioxidant results, both the NPs were also tested for the total reducing power assay. The premise behind the reducing power technique is that compounds with reduction potential engage with potassium ferricyanide (Fe^{3+}) to generate potassium ferrocyanide (Fe^{2+}), which then interacts with ferric chloride to form a ferric-ferrous complex [65]. Likewise, Co_9S_8-NPs exhibited excellent antioxidant capacity which was calculated as 239.87±1.8 µg AAE/mg. Contrary,

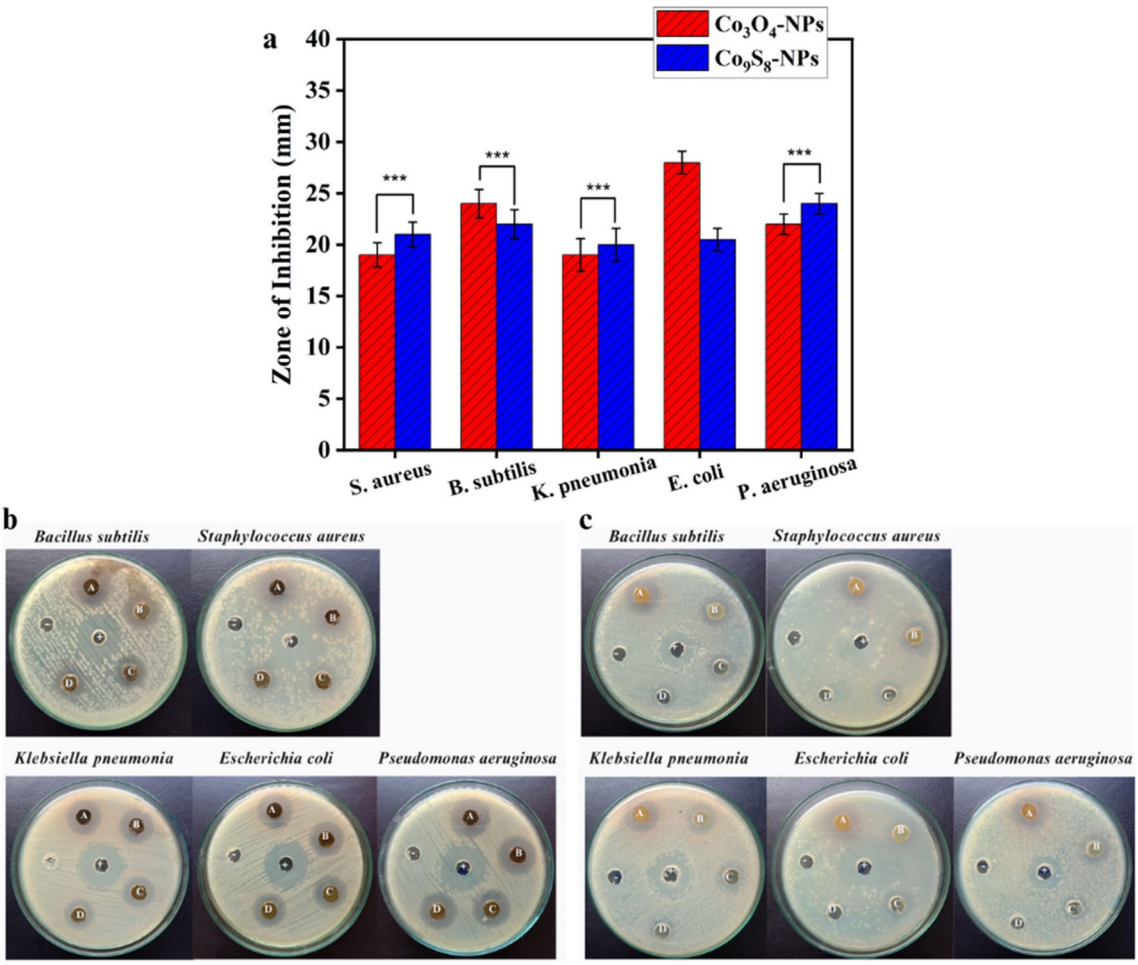

Fig. 7 Graphical representation of the antibacterial activity of **a** Co_9S_8-NPs and Co_3O_4-NPs (***$P<0.05$) and pictorial presentation of antibacterial activity of **b** Co_9S_8-NPs and **c** Co_3O_4-NPs

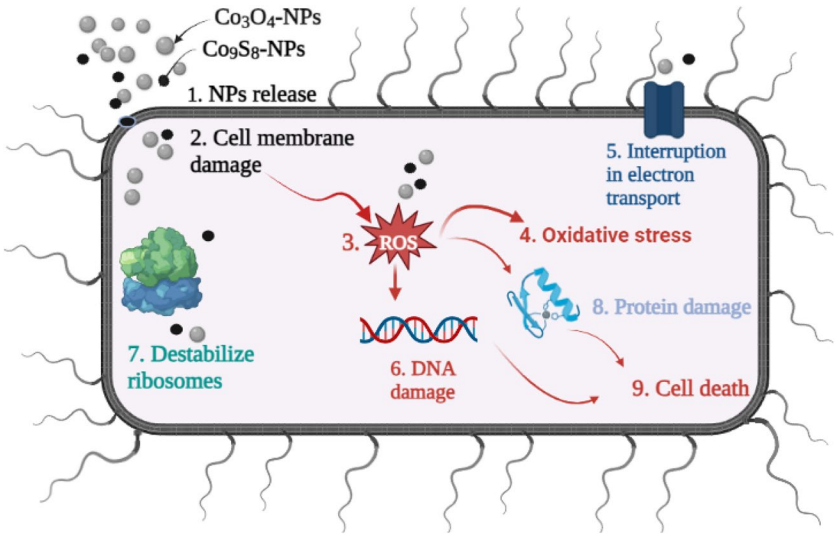

Fig. 8 Graphical illustration of possible antibacterial mechanism of action of Co_3O_4-NPs and Co_9S_8-NPs

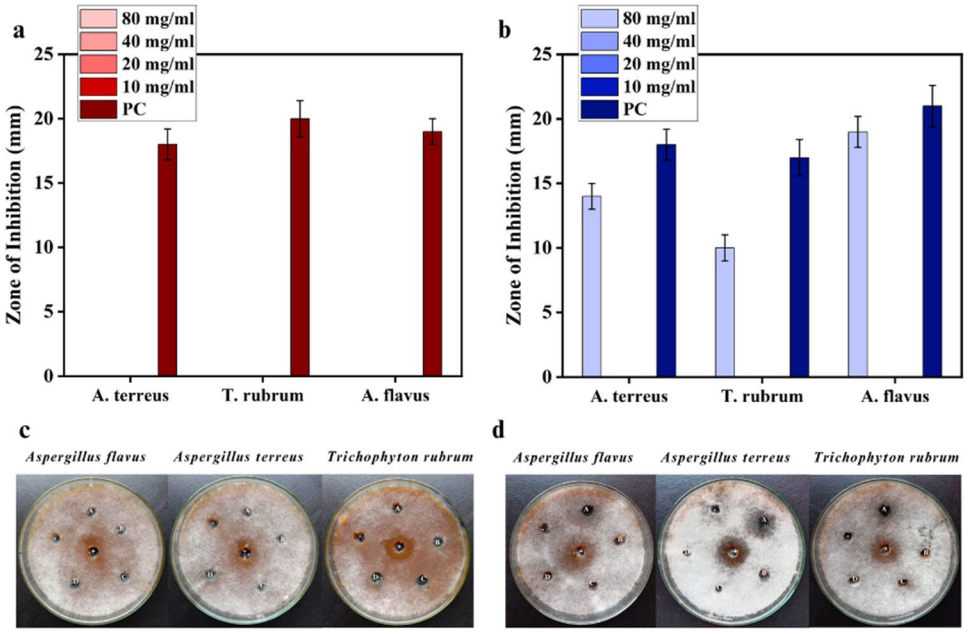

Fig. 9 Graphical representation of the antifungal activity of **a** Co_3O_4-NPs and **b** Co_9S_8-NPs and pictorial presentation of antifungal activity of **c** Co_3O_4-NPs and **d** Co_9S_8-NPs

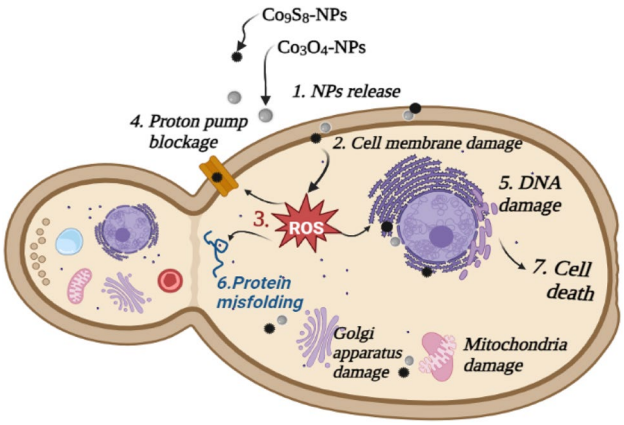

Fig. 10 Graphical illustration of possible antifungal mechanism of action of Co_3O_4-NPs and Co_9S_8-NPs

Co_3O_4-NPs showed comparatively weak antioxidant ability which was calculated as 192.82±1.6 µg AAE/mg. Our study thus concludes that Co_9S_8-NPs exhibit better antioxidant properties as compared to Co_3O_4-NPs.

3.3.5 Biocompatibility

Biocompatibility is an essential aspect of nanomaterials to understand the response of cells or tissues to biomaterials or nanomaterial-based implants [66, 67]. A hemocompatibility assay was performed to analyze the toxicity and compatibility of PEG-coated Co_3O_4-NPs and Co_9S_8-NPs against human red blood cells (RBCs). Different concentrations (5 mg/ml, 2.5 mg/ml, 1.125 mg/ml, and 0.562 mg/ml) of the NPs were tested against RBCs. No hemolytic behavior was shown by NPs even at the highest tested concentrations as displayed in Fig. 14. All the cells retained their integrity

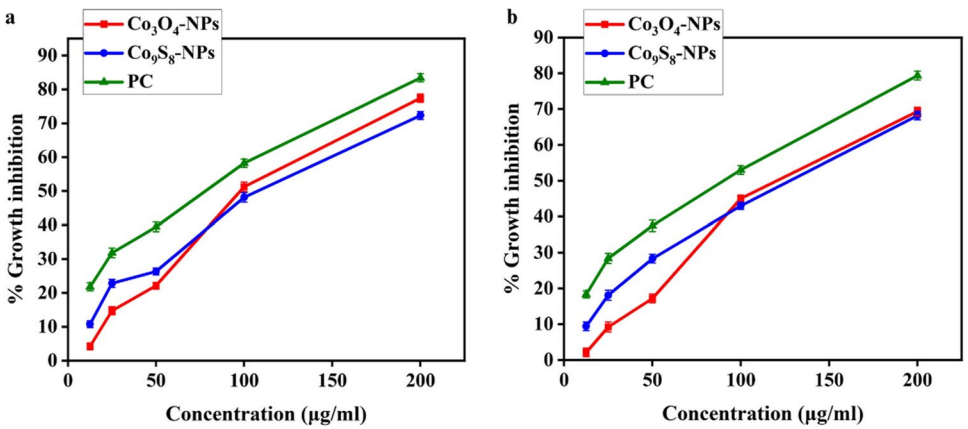

Fig. 11 Antileishmanial activity of Co_3O_4-NPs and Co_9S_8-NPs against **a** promastigotes and **b** amastigotes forms of *Leishmania tropica*

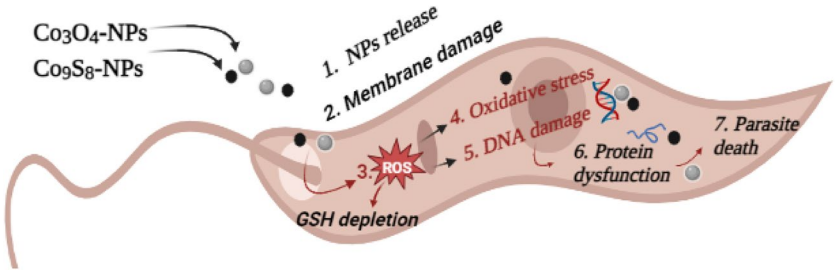

Fig. 12 Graphical illustration of the possible mechanism of action Co_3O_4-NPs and Co_9S_8-NPs against leishmanial cell

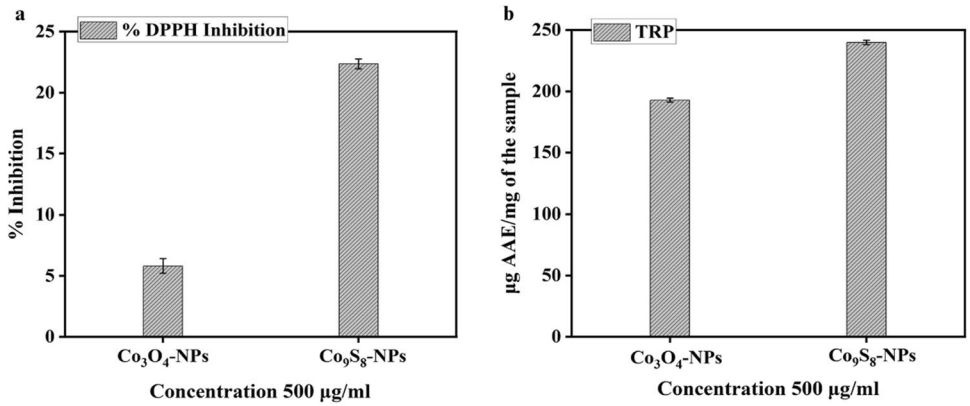

Fig. 13 Graphical presentation of antioxidant activity of Co_3O_4-NPs and Co_9S_8-NPs for **a** DPPH and **b** TRP

and did not rupture during the co-incubation with nanoparticles. Contrary to nanoparticles, Triton X-100 which was employed as a positive control showed complete hemolysis of RBCs as can be visualized in the figure. Our data thus shows that Co_3O_4-NPs and Co_9S_8-NPs at described concentrations are safe and do not cause any blood cell damage.

3.4 Photocatalytic Applications

3.4.1 Dye Degradation Assay

The photocatalytic ability of NPs is extremely important due to their potential applications in energy production and environmental remediation. The nanomaterials, when exposed to a direct source of light (sunlight), can start chemical reactions that break down dye molecules transforming light energy into usable forms, and facilitating the production of valuable compounds [68]. The chemically synthesized PEGylated Co_3O_4-NPs and Co_9S_8-NPs were evaluated for photocatalytic activity against methylene blue dye as summarized in Fig 15. The optimal absorbance peak for MB dye was determined to be at 664 nm. For Co_3O_4-NPs, a sudden drop in peak intensity was observed, after incubation of 120 min, which was indicative of the photocatalytic degradation of dye. It resulted in a 19.87% degradation of MB dye. Interestingly, a constant rise in % dye degradation was observed, as the time interval moved from 120 to 180 min. Incubation of MB dye with Co_3O_4-NPs, for 180 min, resulted in 46.93% degradation. However, for Co_9S_8-NPs, peak intensity dropped after an incubation period of 30 min and continued to decline until 180 min. The % degradation of MB was 0.286% during the first 30 min of incubation and climbed to 10.29% at 60 min. The % degradation increased up to 42% as the incubation period reached 180 min. This data thus demonstrates that Co_9S_8-NPs displayed prominent sensitivity against dye even at 30 min of incubation while Co_3O_4-NPs were not very sensitive at a low incubation period as they showed significant sensitivity after 120 min of incubation.

A comprehensive literature review shows that when NPs interact with the dye, they allow dye molecules to adsorb on the surface of NPs due to the high surface-to-volume ratio of the NPs as depicted in Fig 16. The NPs then start producing reactive oxygen species (ROS) such as ·OH and $\cdot O_2^-$ through photoactivation or in the presence of sunlight. The ROS in turn initiates oxidative reactions, thus destroying the molecular structure of dye molecules. As NPs are excellent catalysts, they speed up the dye degradation process by providing multiple additional active binding sites to dye molecules. Denaturation of dye molecules also leads to discoloration of the dye [49].

$$Co_3O_4 - \text{NPs or } Co_9S_8 - \text{NPs} + h\nu \text{ (light energy)} \square Co_3O_4 \text{ or } Co_9S_8 \left(e^-_{\text{conduction band}} + h^+_{\text{valance band}}\right)$$

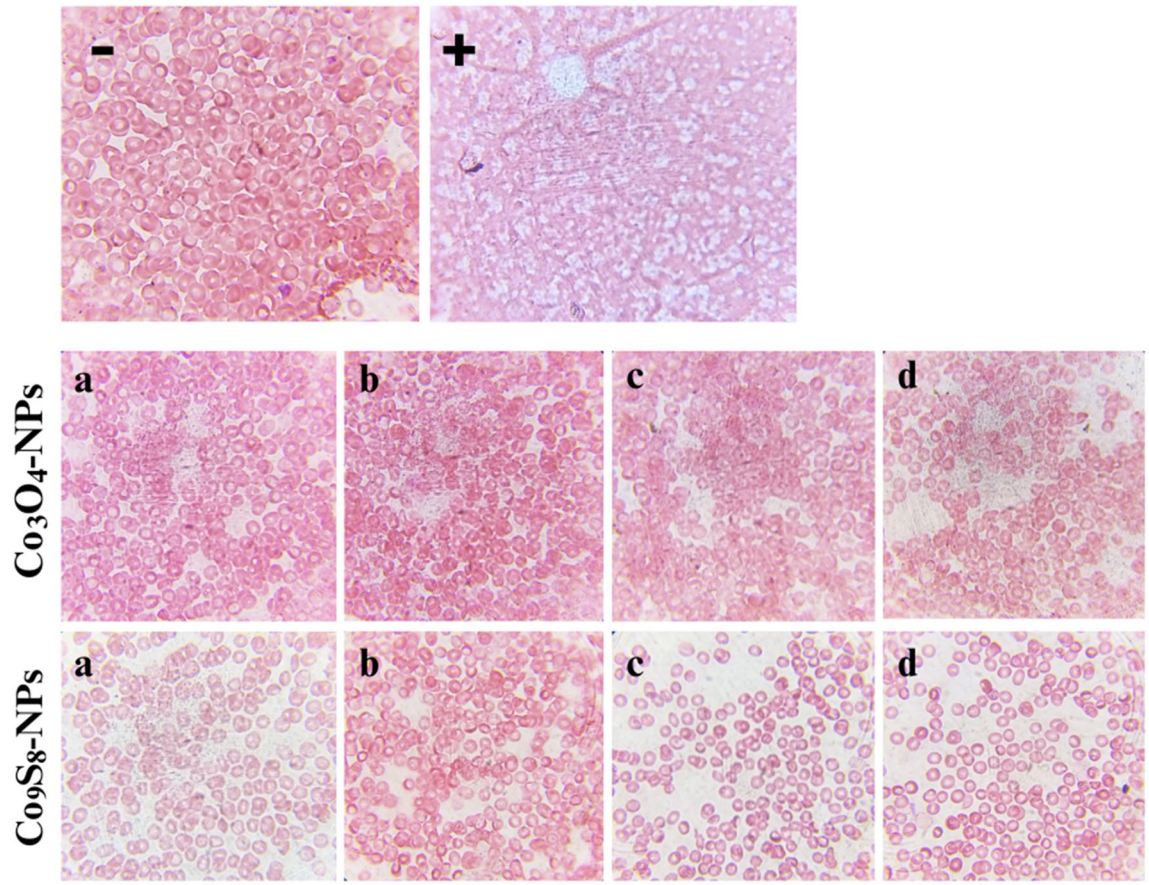

Fig. 14 Microscopic observation of blood cells treated with different concentrations of Co_3O_4-NPs and Co_9S_8-NPs at 1000×

$$h^{+}_{(\text{valance band})} + H_2O\square OH. + H^{+}$$

$$e^{-}_{(\text{conduction band})} + O_2\square{-}O_2$$

$$(-O_2) + H_2O\square H_2O_2 + OH$$

$$H_2O_2\square 2OH$$

$$OH\bullet + \text{MB dye}\square CO_2 + H_2O \text{ (Degradation products)}$$

4 Conclusion

The current study aimed to compare the biological and photocatalytic properties of PEGylated Co_3O_4-NPs and Co_9S_8-NPs synthesized via a facile co-precipitation approach. XRD and SEM analysis determined the phase structure, crystalline nature, and elliptical/irregularly shaped morphology of both the NPs while EDX affirmed the presence of Co, O, and S in respective samples. FTIR analysis also confirmed the successful capping of poly(ethylene glycol) onto the surface of both the NPs. The biological studies carried out in the study revealed that PEGylated Co_9S_8-NPs exhibit better antioxidant, antibacterial, antifungal, and antileishmanial properties as compared to Co_3O_4-NPs. Furthermore, both the NPs demonstrated excellent in vitro compatibility against isolated red blood cells, thus showing the compatible and bio-safe nature of the particles. However, Co_3O_4-NPs possessed slightly improved photocatalytic degradation of methylene blue (MB) dye as compared to Co_9S_8-NPs. Our study thus demonstrated that biocompatible PEGylated Co_3O_4-NPs and Co_9S_8-NPs possess excellent biological and catalytic properties and thus could be further explored for *in vivo* biomedical and remediation applications.

Declarations

Competing Interests The authors declare no competing interests.

Informed Consent Not applicable

Conflict of Interest The authors declare no competing interests.

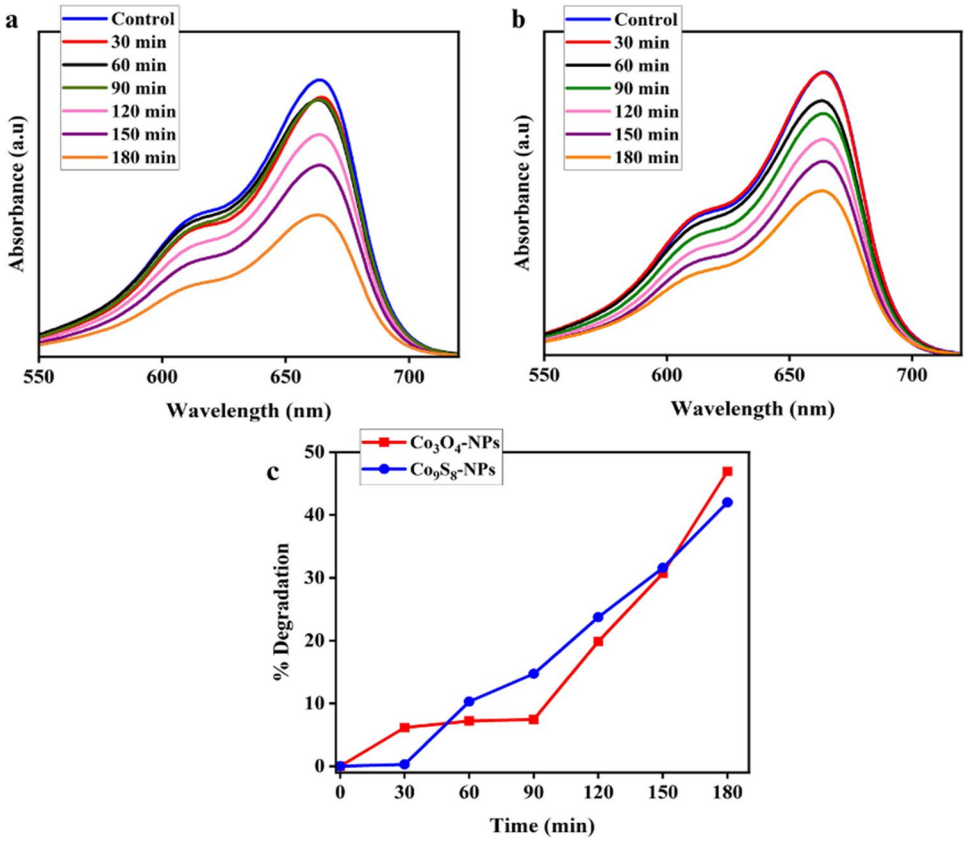

Fig. 15 Photocatalytic degradation of MB dye at varying time intervals by **a** Co_3O_4-NPs, **b** Co_9S_8-NPs, and **c** % dye degradation at 664 nm (λ)

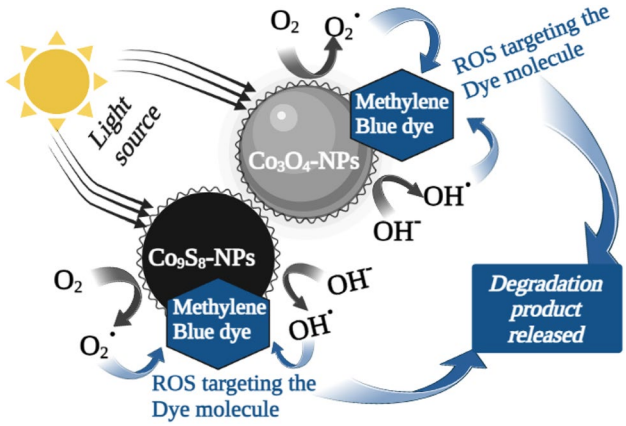

Fig. 16 Graphical illustration of the possible mechanism of methylene blue (MB) degradation by Co_3O_4-NPs and Co_9S_8-NPs

Research Involving Humans and Animals Statement None

References

1. Khalil, A. T., Ovais, M., Ullah, I., et al. (2020). Bioinspired synthesis of pure massicot phase lead oxide nanoparticles and assessment of their biocompatibility, cytotoxicity and in-vitro biological properties. *Arabian Journal of Chemistry, 13*, 916–931. https://doi.org/10.1016/J.ARABJC.2017.08.009
2. Akram, R., Khan, M. D., Zequine, C., et al. (2020). Cobalt sulfide nanoparticles: Synthesis, water splitting and supercapacitance studies. *Materials Science in Semiconductor Processing, 109*, 104925. https://doi.org/10.1016/J.MSSP.2020.104925
3. Rahimi-Nasrabadi, M., Naderi, H. R., Karimi, M. S., et al. (2017). Cobalt carbonate and cobalt oxide nanoparticles synthesis, characterization and supercapacitive evaluation. *Journal of Materials Science: Materials in Electronics, 28*, 1877–1888. https://doi.org/10.1007/s10854-016-5739-z
4. Salimi, A., Mamkhezri, H., Hallaj, R., & Soltanian, S. (2008). Electrochemical detection of trace amount of arsenic(III) at glassy carbon electrode modified with cobalt oxide nanoparticles. *Sensors and Actuators B: Chemical, 129*, 246–254. https://doi.org/10.1016/j.snb.2007.08.017
5. Abudayyak, M., Gurkaynak, T. A., & Özhan, G. (2017). In vitro evaluation of cobalt oxide nanoparticle-induced toxicity. *Toxicology and Industrial Health, 33*, 646–654. https://doi.org/10.1177/0748233717706633
6. Ramachandran, R., Felix, S., Saranya, M., et al. (2013). Synthesis of cobalt sulfide-graphene (CoS/G) nanocomposites for supercapacitor applications. *IEEE Transactions on Nanotechnology, 12*. https://doi.org/10.1109/TNANO.2013.2278287
7. Liu, Y., Jiang, W., Liu, M., et al. (2019). Ultrafine Co1–x S attached to porous interconnected carbon skeleton for sodium-ion batteries. *Langmuir, 35*, 16487–16495. https://doi.org/10.1021/acs.langmuir.9b03051
8. Yang, J., Zhang, Y., Sun, C., et al. (2015). Controlled synthesis of zinc cobalt sulfide nanostructures in oil phase and their potential applications in electrochemical energy storage. *Journal*

of Materials Chemistry A, 3, 11462–11470. https://doi.org/10.1039/C5TA01739D
9. Qu, B., Chen, Y., Zhang, M., et al. (2012). β-Cobalt sulfide nanoparticles decorated graphene composite electrodes for high capacity and power supercapacitors. *Nanoscale, 4*, 7810. https://doi.org/10.1039/c2nr31902k
10. Hafeez, M., Shaheen, R., Akram, B., et al. (2020). Green synthesis of cobalt oxide nanoparticles for potential biological applications. *Materials Research Express, 7*, 025019. https://doi.org/10.1088/2053-1591/ab70dd
11. Haq, S., Abbasi, F., Ben Ali, M., et al. (2021). Green synthesis of cobalt oxide nanoparticles and the effect of annealing temperature on their physiochemical and biological properties. *Materials Research Express, 8*, 075009. https://doi.org/10.1088/2053-1591/ac1187
12. Rajeswari, V. D., Khalifa, A. S., Elfasakhany, A., et al. (2023). Green and ecofriendly synthesis of cobalt oxide nanoparticles using Phoenix dactylifera L: antimicrobial and photocatalytic activity. *Applied Nanoscience, 13*, 1367–1375. https://doi.org/10.1007/s13204-021-02038-5
13. Ajarem, J. S., Maodaa, S. N., Allam, A. A., et al. (2022). Benign synthesis of cobalt oxide nanoparticles containing red algae extract: Antioxidant, antimicrobial, anticancer, and anticoagulant activity. *Journal of Cluster Science, 33*, 717–728. https://doi.org/10.1007/s10876-021-02004-9
14. Shanmuganathan, R., Sathiyavimal, S., Hoang Le, Q., et al. (2023). Green synthesized cobalt oxide nanoparticles using Curcuma longa for anti-oxidant, antimicrobial, dye degradation and anti-cancer property. *Environmental Research, 236*, 116747. https://doi.org/10.1016/j.envres.2023.116747
15. Anuradha, C. T., & Raji, P. (2021). Citrus limon fruit juice-assisted biomimetic synthesis, characterization and antimicrobial activity of cobalt oxide (Co3O4) nanoparticles. *Applied Physics A: Materials Science & Processing, 127*, 55. https://doi.org/10.1007/s00339-020-04209-7
16. Salavati-Niasari, M., Khansari, A., & Davar, F. (2009). Synthesis and characterization of cobalt oxide nanoparticles by thermal treatment process. *Inorganica Chimica Acta, 362*, 4937–4942. https://doi.org/10.1016/j.ica.2009.07.023
17. Bibi, I., Nazar, N., Iqbal, M., et al. (2017). Green and eco-friendly synthesis of cobalt-oxide nanoparticle: Characterization and photo-catalytic activity. *Advanced Powder Technology, 28*, 2035–2043. https://doi.org/10.1016/j.apt.2017.05.008
18. Khan, S., Ansari, A. A., Khan, A. A., et al. (2015). In vitro evaluation of anticancer and antibacterial activities of cobalt oxide nanoparticles. *JBIC, Journal of Biological Inorganic Chemistry, 20*, 1319–1326. https://doi.org/10.1007/s00775-015-1310-2
19. Kokilavani, S., Syed, A., AL-Shwaiman, H. A., et al. (2021). Preparation of plasmonic CoS/Ag2WO4 nanocomposites: Efficient visible light driven photocatalysts and enhanced antimicrobial activity. *Colloids and Interface Science Communications, 42*, 100415. https://doi.org/10.1016/j.colcom.2021.100415
20. Iqbal, J., Abbasi, B. A., Batool, R., et al. (2019). Biogenic synthesis of green and cost effective cobalt oxide nanoparticles using Geranium wallichianum leaves extract and evaluation of in vitro antioxidant, antimicrobial, cytotoxic and enzyme inhibition properties. *Materials Research Express, 6*, 115407. https://doi.org/10.1088/2053-1591/AB4F04
21. Nafari, A., Cheraghipour, K., Sepahvand, M., et al. (2020). Nanoparticles: new agents toward treatment of leishmaniasis. *Parasite Epidemiology and Control, 10*, e00156. https://doi.org/10.1016/j.parepi.2020.e00156
22. Jeevanandam, J., Chan, Y. S., Pan, S., & Danquah, M. K. (2019). Metal oxide nanocomposites: cytotoxicity and targeted drug delivery applications. *Hybrid Nanocomposites: Fundamentals, Synthesis and Applications*, 111–147. https://doi.org/10.1201/9780429000966-3
23. Xue, G., Bai, T., Wang, W., et al. (2022). Recent advances in various applications of nickel cobalt sulfide-based materials. *Journal of Materials Chemistry A, 10*, 8087–8106. https://doi.org/10.1039/D2TA00305H
24. Guan, G., Wang, X., Huang, X., et al. (2018). Porous cobalt sulfide hollow nanospheres with tunable optical property for magnetic resonance imaging-guided photothermal therapy. *Nanoscale, 10*, 14190–14200. https://doi.org/10.1039/C8NR01926F
25. Yuan, M., Xu, S., Zhang, Q., et al. (2020). Bicompatible porous Co3O4 nanoplates with intrinsic tumor metastasis inhibition for multimodal imaging and DNA damage–mediated tumor synergetic photothermal/photodynamic therapy. *Chemical Engineering Journal, 394*, 124874. https://doi.org/10.1016/j.cej.2020.124874
26. Lin, S., Wang, Y., Chen, Z., et al. (2018). Biomineralized enzyme-like cobalt sulfide nanodots for synergetic phototherapy with tumor multimodal imaging navigation. *ACS Sustainable Chemistry & Engineering, 6*, 12061–12069. https://doi.org/10.1021/acssuschemeng.8b02386
27. Li, Z., Li, Z., Chen, L., et al. (2018). Polyethylene glycol-modified cobalt sulfide nanosheets for high-performance photothermal conversion and photoacoustic/magnetic resonance imaging. *Nano Research, 11*, 2436–2449. https://doi.org/10.1007/s12274-017-1865-z
28. Novotna, B., Herynek, V., Rossner, P., et al. (2017). The effects of grafted mesenchymal stem cells labeled with iron oxide or cobalt-zinc-iron nanoparticles on the biological macromolecules of rat brain tissue extracts. *International Journal of Nanomedicine, 12*, 4519–4526. https://doi.org/10.2147/IJN.S133156
29. Khoshroo, A., Mazloum-Ardakani, M., & Forat-Yazdi, M. (2018). Enhanced performance of label-free electrochemical immunosensor for carbohydrate antigen 15-3 based on catalytic activity of cobalt sulfide/graphene nanocomposite. *Sensors and Actuators B: Chemical, 255*, 580–587. https://doi.org/10.1016/j.snb.2017.08.114
30. Li, J., Liu, Y., Tang, X., et al. (2020). Multiwalled carbon nanotubes coated with cobalt(II) sulfide nanoparticles for electrochemical sensing of glucose via direct electron transfer to glucose oxidase. *Microchimica Acta, 187*, 80. https://doi.org/10.1007/s00604-019-4047-8
31. Yang, Z., Zhu, Y., Chi, M., et al. (2018). Fabrication of cobalt ferrite/cobalt sulfide hybrid nanotubes with enhanced peroxidase-like activity for colorimetric detection of dopamine. *Journal of Colloid and Interface Science, 511*, 383–391. https://doi.org/10.1016/j.jcis.2017.09.097
32. Kristl, M., Dojer, B., Gyergyek, S., & Kristl, J. (2017). Synthesis of nickel and cobalt sulfide nanoparticles using a low cost sonochemical method. *Heliyon, 3*. https://doi.org/10.1016/j.heliyon.2017.e00273
33. Bloch, K., Pardesi, K., Satriano, C., & Ghosh, S. (2021). Bacteriogenic platinum nanoparticles for application in nanomedicine. *Frontiers in Chemistry, 9*, 624344. https://doi.org/10.3389/fchem.2021.624344
34. Paul, B., Bhanja, P., Sharma, S., et al. (2021). Morphologically controlled cobalt oxide nanoparticles for efficient oxygen evolution reaction. *Journal of Colloid and Interface Science, 582*, 322–332. https://doi.org/10.1016/j.jcis.2020.08.029
35. Emadi, H., Salavati-Niasari, M., & Davar, F. (2012). Synthesis and characterization of cobalt sulfide nanocrystals in the presence of thioglycolic acid via a simple hydrothermal method. *Polyhedron, 31*, 438–442. https://doi.org/10.1016/j.poly.2011.09.047
36. Jevševar, S., Kunstelj, M., & Porekar, V. G. (2010). PEGylation of therapeutic proteins. *Biotechnology Journal, 5*, 113–128. https://doi.org/10.1002/biot.200900218

37. Veronese, F. M., & Pasut, G. (2005). PEGylation, successful approach to drug delivery. *Drug Discovery Today, 10*, 1451–1458. https://doi.org/10.1016/S1359-6446(05)03575-0
38. Yadav, I., Purohit, S. D., Singh, H., et al. (2021). A highly transparent tri-polymer complex in situ hydrogel of HA, collagen and four-arm-PEG as potential vitreous substitute. *Biomedical Materials, 16*, 065018. https://doi.org/10.1088/1748-605X/ac2714
39. Jegatheeswaran, S., & Sundrarajan, M. (2015). PEGylation of novel hydroxyapatite/PEG/Ag nanocomposite particles to improve its antibacterial efficacy. *Materials Science and Engineering: C, 51*, 174–181. https://doi.org/10.1016/j.msec.2015.02.012
40. Bastos, V., Ferreira de Oliveira, J. M. P., Brown, D., et al. (2016). The influence of citrate or PEG coating on silver nanoparticle toxicity to a human keratinocyte cell line. *Toxicology Letters, 249*, 29–41. https://doi.org/10.1016/j.toxlet.2016.03.005
41. Nicosia, A., Abbadessa, A., Vento, F., et al. (2021). Silver nanoparticles decorated with PEGylated porphyrins as potential theranostic and sensing agents. *Materials (Basel), 14*, 2764. https://doi.org/10.3390/ma14112764
42. Sadalage, P. S., Patil, R. V., Havaldar, D. V., et al. (2021). Optimally biosynthesized, PEGylated gold nanoparticles functionalized with quercetin and camptothecin enhance potential anti-inflammatory, anti-cancer and anti-angiogenic activities. *Journal of Nanobiotechnology, 19*, 84. https://doi.org/10.1186/s12951-021-00836-1
43. Saikumari, N., Dev, S. M., & Dev, S. A. (2021). Effect of calcination temperature on the properties and applications of bio extract mediated titania nano particles. *Scientific Reports, 11*, 1734. https://doi.org/10.1038/s41598-021-80997-z
44. Munir, T., ur Rehman, N., Mahmood, A., et al. (2020). Structural, optical, electrical and thermo-electrical properties of Cu doped Co9S8-NPs synthesized via co-precipitation method. *Chemical Physics Letters, 761*, 137989. https://doi.org/10.1016/j.cplett.2020.137989
45. Vijayakumar, S., Mahadevan, S., Arulmozhi, P., et al. (2018). Green synthesis of zinc oxide nanoparticles using Atalantia monophylla leaf extracts: Characterization and antimicrobial analysis. *Materials Science in Semiconductor Processing, 82*, 39–45. https://doi.org/10.1016/j.mssp.2018.03.017
46. Khan, A. U., Khan, H. U., Alhar, M. S. O., et al. (2023). Antimicrobial, antioxidant, and antileishmanial activity of Tavernier glabra mediated ZnO NPs and Fe2O3 NPs. *Inorganic Chemistry Communications, 148*, 110297. https://doi.org/10.1016/j.inoche.2022.110297
47. Ihsan, J., Farooq, M., Khan, M. A., et al. (2021). Synthesis, characterization, and biological screening of metal nanoparticles loaded gum acacia microgels. *Microscopy Research and Technique, 84*, 1673–1684. https://doi.org/10.1002/jemt.23726
48. Aziz, S., Abdullah, S., Anwar, H., et al. (2021). Effect of engineered nickel oxide nanoparticles on antioxidant enzymes in freshwater fish, Labeo rohita. *Pakistan Veterinary Journal, 41*, 424–428. https://doi.org/10.29261/pakvetj/2021.044
49. Ghaedi, M., Heidarpour, S., Nasiri Kokhdan, S., et al. (2012). Comparison of silver and palladium nanoparticles loaded on activated carbon for efficient removal of Methylene blue: Kinetic and isotherm study of removal process. *Powder Technology, 228*, 18–25. https://doi.org/10.1016/j.powtec.2012.04.030
50. Khan, M. A., Siddique, M. A. R., Sajid, M., et al. (2023). A comparative study of green and chemical cerium oxide nanoparticles (CeO2-NPs): From synthesis, characterization, and electrochemical analysis to multifaceted biomedical applications. *Bionanoscience, 13*, 667–685. https://doi.org/10.1007/s12668-023-01114-0
51. Athar, T., Hakeem, A., Topnani, N., & Hashmi, A. (2012). Wet synthesis of monodisperse cobalt oxide nanoparticles. *ISRN Materials Science, 2012*, 1–5. https://doi.org/10.5402/2012/691032
52. Karuppiah, S., Thangaraj, S., Arunachalam Palaniappan, S., & Olapalayam Lakshmanan, S. (2019). Influence of surfactants on structural, morphological, optical and antibacterial properties of SnO_2 nanoparticles. *IET Nanobiotechnology, 13*, 952–956. https://doi.org/10.1049/iet-nbt.2019.0095
53. Boccuzzi, F., Chiorino, A., & Manzoli, M. (2000). FTIR study of the electronic effects of CO adsorbed on gold nanoparticles supported on titania. *Surface Science, 454–456*, 942–946. https://doi.org/10.1016/S0039-6028(00)00160-6
54. Manigandan, R., Giribabu, K., Suresh, R., Vijayalakshmi, L., Stephen, A., & Narayanan, V. (2013). Cobalt oxide nanoparticles: Characterization and its electrocatalytic activity towards nitrobenzene. *Chemical Science Transactions, 2*, S47–S50. https://doi.org/10.7598/cst2013.10
55. Sambathkumar, C., Nallamuthu, N., Kumar, M. K., et al. (2022). Electrochemical exploration of cobalt sulfide nanoparticles synthesis using cobalt diethyldithiocarbamate as single source precursor for hybrid supercapacitor device. *Journal of Alloys and Compounds, 920*, 165839. https://doi.org/10.1016/j.jallcom.2022.165839
56. Muradov, M. B., Balayeva, O. O., Azizov, A. A., et al. (2018). Synthesis and characterization of cobalt sulfide nanoparticles by sonochemical method. *Infrared Physics & Technology, 89*, 255–262. https://doi.org/10.1016/j.infrared.2018.01.014
57. Balasubramanian, R., Kim, B., Tripp, S. L., et al. (2002). Dispersion and stability studies of resorcinarene-encapsulated gold nanoparticles. *Langmuir, 18*, 3676–3681. https://doi.org/10.1021/la0156107
58. Andra S, Satheesh Kumar Balu &, Jeevanandam J, Muthalagu M (2021) Emerging nanomaterials for antibacterial textile fabrication. Naunyn-Schmiedeberg's Archives of Pharmacology 394:1355–1382. https://doi.org/10.1007/s00210-021-02064-8/Published
59. Shaikh, S., Nazam, N., Rizvi, S. M. D., et al. (2019). Mechanistic insights into the antimicrobial actions of metallic nanoparticles and their implications for multidrug resistance. *International Journal of Molecular Sciences, 20*, 2468. https://doi.org/10.3390/ijms20102468
60. Xu, Y., Wei, M.-T., Ou-Yang, H. D., et al. (2016). Exposure to TiO2 nanoparticles increases Staphylococcus aureus infection of HeLa cells. *Journal of Nanobiotechnology, 14*, 1–16. https://doi.org/10.1186/s12951-016-0184-y
61. Rudramurthy, S. M., Paul, R. A., Chakrabarti, A., et al. (2019). Invasive Aspergillosis by Aspergillus flavus: Epidemiology, diagnosis, antifungal resistance, and management. *Journal of Fungus, 5*, 55. https://doi.org/10.3390/jof5030055
62. Cruz-Luna, A. R., Cruz-Martínez, H., Vásquez-López, A., & Medina, D. I. (2021). Metal nanoparticles as novel antifungal agents for sustainable agriculture: Current advances and future directions. *Journal of Fungus, 7*, 1033. https://doi.org/10.3390/jof7121033
63. Allahverdiyev, A. M., Abamor, E. S., Bagirova, M., et al. (2013). Investigation of antileishmanial activities of Tio2@Ag nanoparticles on biological properties of L. tropica and L. infantum parasites, in vitro. *Experimental Parasitology, 135*, 55–63. https://doi.org/10.1016/j.exppara.2013.06.001
64. Baliyan, S., Mukherjee, R., Priyadarshini, A., et al. (2022). Determination of antioxidants by DPPH radical scavenging activity and quantitative phytochemical analysis of Ficus religiosa. *Molecules, 27*, 1326. https://doi.org/10.3390/molecules27041326

65. Bhalodia, N., Nariya, P., Shukla, V., & Acharya, R. (2013). In vitro antioxidant activity of hydro alcoholic extract from the fruit pulp of Cassia fistula Linn. *AYU (An International Quarterly Journal of Research in Ayurveda), 34*, 209. https://doi.org/10.4103/0974-8520.119684
66. Laloy, J., Minet, V., Alpan, L., et al. (2014). Impact of silver nanoparticles on haemolysis, platelet function and coagulation. *Nanobiomedicine, 1*, 4. https://doi.org/10.5772/59346
67. Farooq, M., Ihsan, J., Mohamed, R. M., et al. (2022). Highly biocompatible formulations based on Arabic gum nano composite hydrogels: Fabrication, characterization, and biological investigation. *International Journal of Biological Macromolecules, 209*, 59–69. https://doi.org/10.1016/j.ijbiomac.2022.03.162
68. Hermosilla, E., Díaz, M., Vera, J., et al. (2022). Molecular weight identification of compounds involved in the fungal synthesis of AgNPs: Effect on antimicrobial and photocatalytic activity. *Antibiotics, 11*, 622. https://doi.org/10.3390/antibiotics11050622